Proceedings of Tailings and Mine Waste 2024
November 10–13, 2024, Colorado, USA

Assessing SAR, InSAR and Multispectral Optical Data for Mapping Supernatant Pond Evolution

Élyse Gaudreau, TRE Altamira Inc., Canada
Ajinkya Koleshwar, TRE Altamira Inc., Canada
Kenny Yue, TRE Altamira Inc., Canada
Pablo Blanco, TRE Altamira Inc., Spain
Riccardo Tortini, TRE Altamira Inc., Canada
Giacomo Falorni, TRE Altamira Inc., Canada

Abstract

The effective management of mine Tailings Storage Facilities (TSF) is a high priority for mine operators, communities, and governments to mitigate the risks associated with water contamination, pollution, and dam failures. The Global Industry Standard on Tailings Management (GISTM) guidelines identify TSF water management as a key requirement for the safety of mining operations. Commonly used methods for monitoring the location and spatial extent of surficial moisture and supernatant ponding within TSFs include the use of multispectral optical satellite imagery. This application requires high accuracy in identifying small water bodies and frequent updates due to the high dynamicity of mining operations; however, freely accessible imagery from Sentinel-2 and Landsat satellites have a pixel resolution of 10 to 20 m and 30 m, respectively, and the temporal coverage can be affected by the presence of cloud cover, illumination differences, and terrain shadow. These limitations can be overcome using high-resolution Synthetic Aperture Radar (SAR) amplitude satellite data, as SAR signals can penetrate cloud cover.

In this study, machine learning techniques are used to characterize TSF saturation changes by combining both Sentinel-2 optical images and high-resolution (3 m) TerraSAR-X SAR data. This study investigates (i) the differences between the supernatant pond areas classified using multiple satellite data sources (SAR amplitude and multispectral optical imagery), (ii) the factors driving the accuracy of SAR water maps in TSF impoundments, and (iii) developing guidelines for the combined use of optical, SAR, and InSAR data for TSF water mapping.

Mapping TSF supernatant water bodies solely with Synthetic Aperture Radar (SAR) data presents major challenges since fully saturated sediments or slurry often appear indistinguishable from water bodies in SAR amplitude data. However, we find that optical, SAR, and InSAR data complement each other well for water body mapping and provide a substantial improvement over the use of each input individually.

High-resolution SAR can provide detailed water body maps over time and space, and when available, cloud- and shadow-free multispectral water indices are reliable indicators of surface water to use as refinement and validation.

Introduction

Mine tailings are the finely ground residuals, including heavy metals and toxins, that remain after the mill process has removed the valuable metals from the ore. Tailings are typically stored permanently in tailings storage facilities (TSFs), ground impoundments retained by dams. The effective management of TSF supernatant ponds (that form due to process and pumped water and natural precipitation) is critical for mine operators, the environment, and communities that would be affected by a dam failure. Different tailings dam databases (ICOLD, WISE, World Mine Tailings Failures, CSP) indicate that, since 1915, a total of 257 failures have been recorded with circa 2,650 fatalities and 250 Mm^3 of contaminated residues released to the environment (Piciullo et al., 2022). As attested to by the different analyses and investigations, the control of water stored inside the TSF reservoir area is a critical issue (Cacciuttolo and Cano, 2023). The Global Industry Standard on Tailings Management (GISTM) guidelines, published in August 2020, also identifies TSF water management as one of the main requirements for the safety of mining operations. In this framework, TSF supernatant pond maps can be effective operational tools for mine operators to identify unexpected or unpredicted behaviors that may contribute to embankment failure.

Remote sensing methods provide cost-effective ways of monitoring water bodies and the saturation levels of tailings facilities over large areas (e.g., Koleshwar et al., 2023), particularly with freely available datasets such as the European Space Agency's Sentinel-1 Synthetic Aperture Radar (SAR) satellite and the Sentinel-2 satellites' multispectral (MS) sensors, as well as the National Aeronautics and Space Administration and United States Geological Survey's MS Landsat sensor. These platforms image most of the surface of the Earth at regular intervals, providing up-to-date data without the need for in-situ measurements or instrumentation.

SAR satellites are active, meaning they emit radar pulses and detect the energy backscattered off the ground. The amplitude of the measured signal represents the fraction of the emitted signal that is reflected in the direction of the satellite and can be used to identify features on the ground. The phase of the returning signal is a function of the distance travelled, and by combining the phase data of successive acquisitions, Interferometric SAR (InSAR) can be used to map ground displacements at a precision on the order of millimeters (Ferretti et al., 2011; Ferretti, 2014). In contrast, MS sensors are passive, and measure the radiation emitted by the sun that reflects off the Earth's surface in the direction of the satellite. While SAR platforms emit and detect a specific wavelength of the electromagnetic spectrum, MS sensors detect a stack

of images with each acquisition, each representing the total reflected energy within a specific band of the electromagnetic spectrum.

The most well-established remote sensing methods of mapping of water bodies and saturation levels use MS data, as different bands of the electromagnetic spectrum have different reflective properties over various types of material such as water, dry soil and vegetation, allowing for land cover classification (e.g., Townshend et al., 1991). These methods include the use of water and moisture indices such as normalized difference water index (NDWI), modified normalized difference water index (MNDWI) and normalized difference moisture index (NDMI) (e.g., Gao, 1996; Xu, 2006; Acharya et al., 2018). For example, the NDWI exploits the contrast in reflectance values of green (500 – 600 nm wavelength) and near-infrared (700 – 1,400 nm wavelength) radiation over water bodies and dry material. One of the main limitations of MS sensors is that electromagnetic radiation at these wavelengths does not penetrate through cloud cover, which can result in lengthy and/or regular temporal data gaps in certain parts of the world. However, SAR satellites operate at wavelengths that are capable of imaging the Earth's surface in any weather, as well as at night.

In this study, we explore the feasibility of using SAR amplitude data to monitor the extent of supernatant ponds using a machine learning (ML; using k-means clustering) and Deep Learning (DL; with a convolutional neural network; CNN) approaches, as this greatly expands the number of datasets available for remotely monitoring supernatant ponds within TSFs. We apply these algorithms to four anonymized TSFs located in a drought-prone area. Two TSFs (referred to as TSF1 and TSF2) are constructed with an upstream raised method, and two are integrated waste landforms (IWL1 and IWL2). The primary TSFs are purposed for storing waste material produced during mining operations, whereas the IWLs are used for both waste storage and controlled seepage recovery of return water from the primary TSFs to reduce the amount of fresh water required from external sources.

The results obtained using a preliminary CNN algorithm show that SAR imagery can successfully identify combined wet beach and ponding areas. The results also reveal different SAR reflectance behaviors over different TSF materials, providing clear directions for further refinement of the algorithm. Additionally, we demonstrate the compatibility of TSF ponding and saturation mapping and InSAR displacement measurements for monitoring and understanding the relationship between TSF activity and embankment stability.

Data and methods

SAR water body mapping

In this study, supernatant ponds within TSFs are mapped using SAR data from different satellite missions with different polarizations, wavelengths, spatial and temporal resolutions. The polarization refers to the

plane in which the electromagnetic wave of the SAR sensor oscillates (vertical or horizontal). Targets imaged on the ground can have different polarimetric properties which may affect the results of a SAR-based water mapping approach (Brisco et al., 2011). The first dataset is the freely available C-band (5.6-cm wavelength) Sentinel-1 data in the VV polarization (i.e., both emitted and return signal are vertically polarized) from the European Space Agency. Its ground resolution is 20 m × 5 m, and the revisit period is 12 days. The second dataset was also acquired by the Sentinel-1 satellite, but in the VH polarization (i.e., the emitted signal is vertically polarized, and the return signal is horizontally polarized). The third dataset is obtained from the TerraSAR-X satellite constellation in the HH polarization (i.e., both emitted and return signal are horizontally polarized). These are commercial X-band data (3.1-cm wavelength), have a ground resolution of 3 m × 3 m and a revisit period of 11 days. The acquisition period for each dataset is listed in Table 1.

Table 1: Datasets used in this study. ML label refers to dataset used for machine learning-based water mapping. InSAR label refers to dataset used for multi-temporal InSAR analysis

Constellation	Sensor	Wavelength	Resolution (m)	Revisit Period (days)	Geometry	Analysis Period
Sentinel-1	SAR	5.6 cm	20 × 5	12	Descending	2018-12-15 to 2024-02-18 (ML) 2021-01-09 to 2024-02-23 (InSAR)
TerraSAR-X	SAR	3.1 cm	3 × 3	11	Ascending	2018-10-30 to 2023-10-19 (ML) 2021-01-10 to 2024-02-28 (InSAR)
Sentinel-2	MS	543 – 578 nm, 785 – 900 nm, 1,565 – 1,655 nm	10 × 10, 10 × 10, 20 × 20	5	Descending	2018-12-14 to 2024-02-16

The SAR data are first pre-processed (i.e., co-registered, amplitude calibrated/normalized), and a Deep Learning speckle filter is applied to reduce noise (*cfr.* Lattari et al., 2019). Two ML water classification algorithms are then used: (i) a statistical approach using K-means clustering and the Sobel operator (Kanopoulos et al., 1988) to define the location and outline of the pond areas, and (ii) a Convolutional Neural Network (CNN) trained on waterbodies such as lakes and rivers using Sentinel-1 data in the VV polarization and MS images. The CNN uses unfiltered SAR data to increase the spatial resolution of the water classification result. While the differences between the backscattering properties of lakes and TSFs are substantial, the results of the CNN algorithm are expected to provide preliminary insights on the use of SAR for TSF water body mapping and help determine directions to refine a CNN specifically tailored to TSFs. A block diagram of the water classification algorithms is shown in Figure 1A. The output is a

raster map of the probability that a pixel is water. A binary map is then created, in which pixels with a probability greater than 0.9 are classified as water.

The results of the SAR water mapping algorithms are validated using the NDWI derived from the green and near-infrared bands of the Sentinel-2 constellation (Table 1). Therefore, we only process SAR images acquired within 1 day of a cloud-free Sentinel-2 acquisition. The NDWI can range from -1 (i.e., dry ground) to 1 (i.e., water) where there is a short transition between dry ground and supernatant ponding near 0 (Gao, 1996). NDWI water classification was performed using two methods: one with a dynamic threshold selected using k-means clustering, and the other where all pixels with an index value greater than 0.3 are selected (Figure 1B). The latter threshold was selected using the statistical distribution of indices in this dataset and a visual check of true color imagery derived from Sentinel-2 data.

Since SAR amplitude data can have similar backscatter behavior over shallow water and saturated material, we classify pixels corresponding to saturated tailings (moisture levels between dry and standing water) using MNDWI, which uses the green and shortwave infrared bands (central wavelength: 1,610 nm) and also ranges from -1 to 1 for dry ground and water, respectively. Its transition zone from dry ground through wet material to water is wider than with NDWI, therefore its water threshold is typically higher and it can better detect beach wetness. We classify MNDWI index values between 0.1 and 0.6 as saturated material and values greater than 0.6 as supernatant pond based on the statistical distribution of indices in this dataset and a qualitative visual assessment of Sentinel-2 true color imagery).

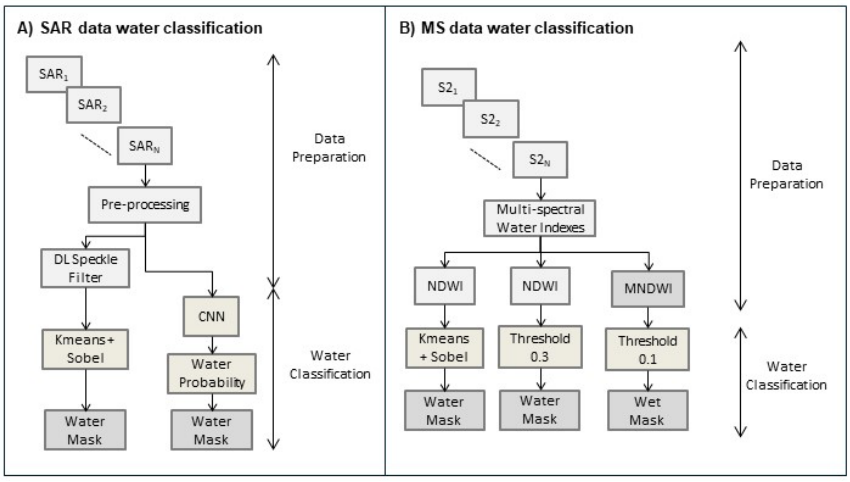

Figure 1: Water classification block diagrams. DL = Deep Learning

Multi-temporal InSAR

Multi-temporal InSAR is a commonly used method for monitoring the stability of TSF embankments. It involves processing dozens to hundreds of SAR phase data acquisitions to extract time series of gradual, millimeter-scale displacements. We use TRE Altamira's proprietary SqueeSAR algorithm to find and follow

natural reflectors on the ground that are statistically reliable throughout the analysis period (Ferretti et al., 2011; Ferretti, 2014). InSAR detects displacements along the satellite line-of-sight (LOS) vector, which "looks" to the right of the satellite's roughly north-south-oriented path. When travelling from south to north (referred to as the "ascending" geometry), the satellite is east-looking. Conversely, when travelling from north to south ("descending" geometry) the satellite is west-looking. We estimate the vertical and east-west components of displacement by decomposing the ascending and descending vectors of displacement occurring at approximately the same time and location.

Results and discussion

Tailings storage facility supernatant pond mapping with synthetic aperture radar

In this section we use the pixels classified as water using NDWI as the reference for the ponding areas. Figures 2a, 2c, 2e and 2g show the time series of the area that was classified as standing water using area within TSF1 and TSF2. The % area within the TSF that has a MNDWI greater than 0.1 (including saturated tailings and ponding areas) is also shown. Figures 3a, 3c, 3e and 3g show the time series of the % area that was classified as standing water using NDWI, saturated material using MNDWI, and the ML statistical (k-means/Sobel) and CNN SAR algorithms, as a percentage of the total TSF and water (ponding) using MNDWI, and the ML statistical (k-means/Sobel) and CNN SAR algorithms, within IWL1 and IWL2, respectively. Some observations are common to all four TSFs: firstly, hardly any pixels of the Sentinel-1 VH-polarized data were classified by the CNN as having a probability of being water greater than 0.9 leading to the % area being 0 or near 0 throughout. We therefore show, for the VH-polarized data only, the % area of pixels with a probability of being water greater than 0.7, and we refer to this dataset for the remainder of the section.

In general, the area classified as water using SAR tends to be greater than the pond area mapped using NDWI. The statistical Sentinel-1 results in the VV polarization are slightly lower and similar to the combined area of saturated material and ponds as mapped by MNDWI, compared to the results from the Sentinel-1 VH polarization and the TerraSAR-X results (HH polarization; Figures 2a, 2e, Figures 3a, 3e). The difference between the VV polarization results and the other two datasets is greater when using the CNN. Furthermore, there are many data acquisitions where the CNN failed to identify any water or saturated material in the VH polarization only. Within TSF1 and TSF2, the statistical and CNN approaches were successful in identifying dry material in the absence of moisture using the VV and HH polarizations (Figure 2a, 2c, 2e, 2g). Starting in September 2022, many dry pixels in TSF1 and TSF2 were identified as water by the statistical and CNN approaches using the VH-polarized data. This is not the case for IWL1 and IWL2, where all datasets were successful at identifying dry pixels in the absence of moisture throughout the

analysis period (Figure 3a, 3c, 3e, 3g). Figure 4 shows an example of the areas classified as water by the different algorithms.

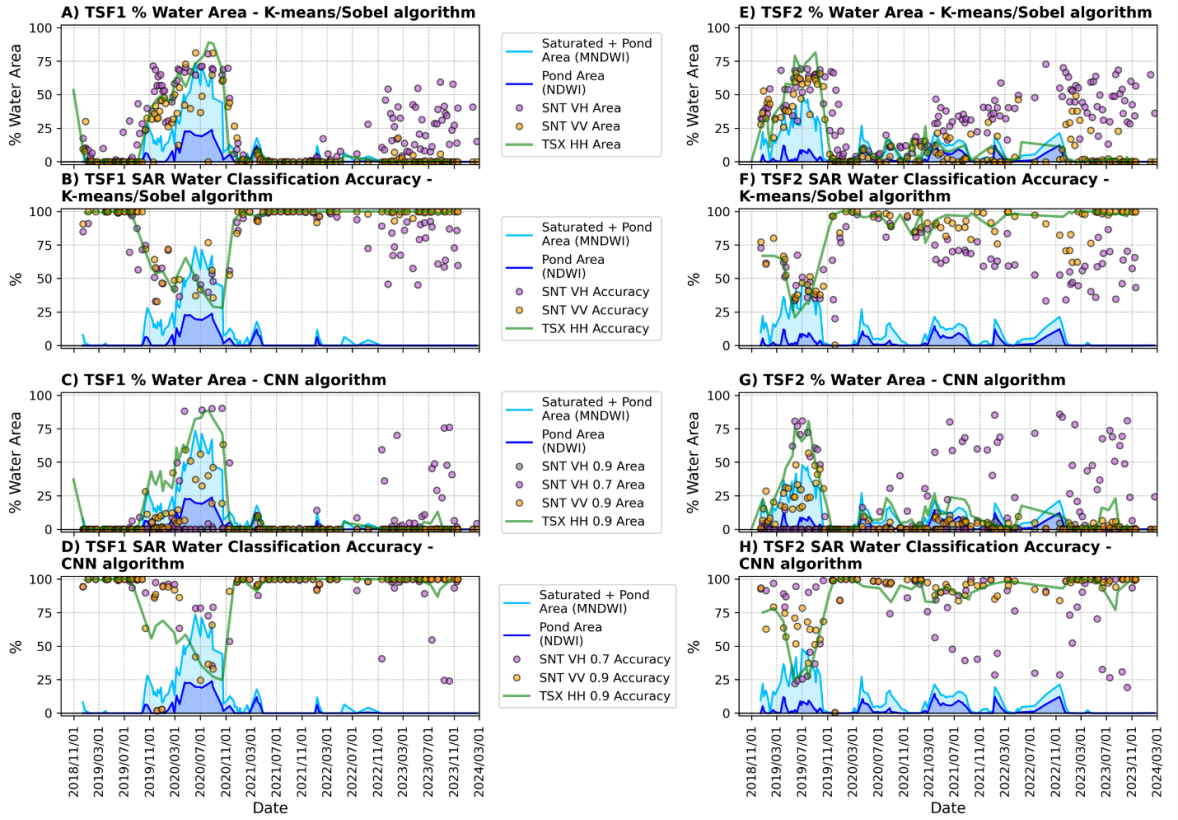

Figure 2: Time series of percentage of tailings storage facility (TSF) area mapped as water using SAR machine learning algorithms and their accuracy. Percentage area of pond and saturated material as measured using normalized difference water indices are shown in each plot as a reference. A-D: TSF1 results. E-H: TSF2 results

The accuracy of the ML algorithms is calculated using a pixel-by-pixel comparison of the SAR and NDWI water masks, with the latter used as the reference for water vs. dry material. Binary SAR water masks are resampled to the same grid as the NDWI masks, and pixels are classified as (i) true positives (TP): SAR and corresponding NDWI pixel are classified as water; (ii) true negatives (TN): SAR and corresponding NDWI pixel are classified as dry; (iii) false positives (FP): SAR pixel classified as water and corresponding NDWI pixel classified as dry; (iv) false negatives (FN): SAR pixel classified as dry and NDWI pixel classified as water. Accuracy is calculated using the following equation:

$$\frac{TP + TN}{TP + TN + FP + FN}$$

Time series of the accuracy of the statistical and CNN SAR water masks for TSF1 and TSF2 are shown in Figures 2b, 2d, 2f and 2h. The accuracy of the statistical water mask is comparable between input

datasets, with high accuracy during dry periods and lower accuracy when there is significant coverage of saturated material, except starting in September 2022 when the Sentinel-1 VH data starts identifying many false positives. The statistical and CNN results are comparable, however in some instances the CNN performs better (e.g. between 11/2019 and 03/2020; Figures 2b and 2d). Note that the higher accuracy of Sentinel-1 VH data during periods with extensive saturation is misleading and is due to the algorithm failing to classify any (or hardly any) pixels as water, resulting in no true positives but still numerous true negatives.

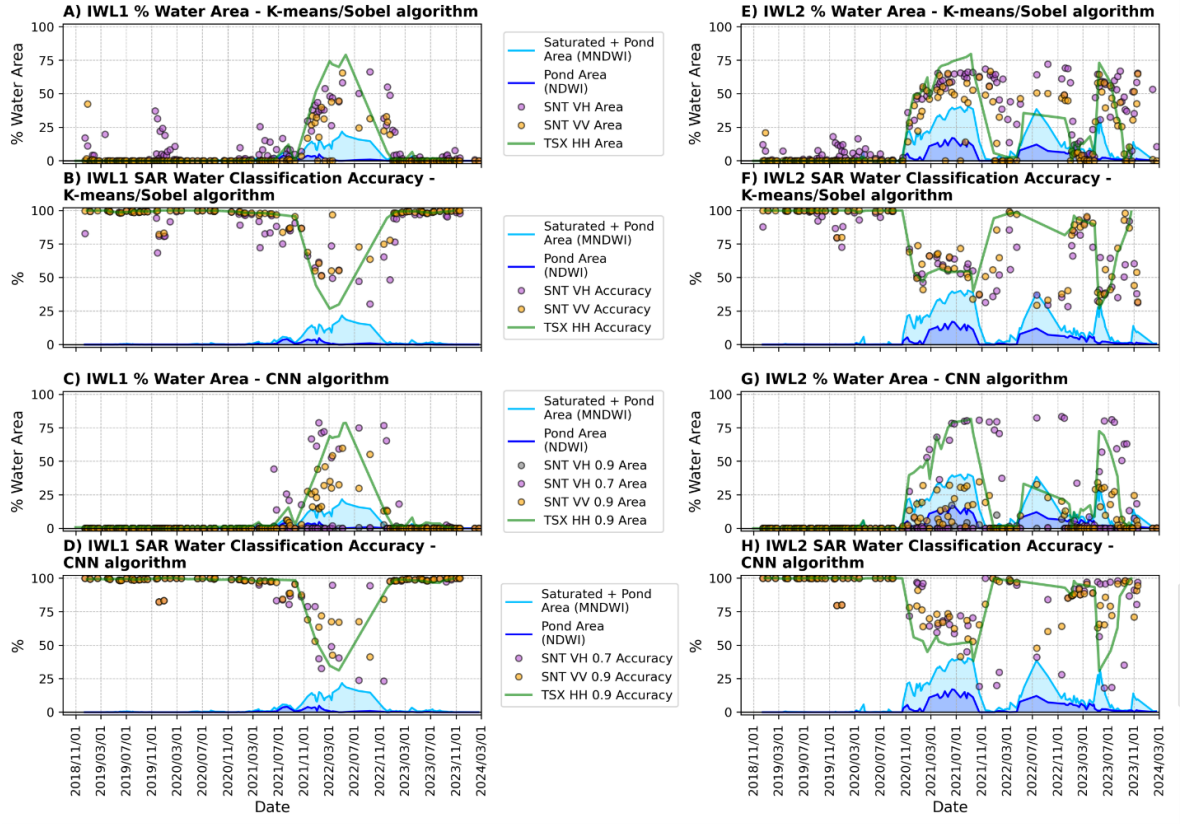

Figure 3: Time series of percentage of integrated waste landform (IWL) area mapped as water using SAR machine learning algorithms and their accuracy. Percentage area of pond and saturated material as measured using normalized difference water indices are shown in each plot as a reference. A-D: IWL1 results. E-H: IWL2 results

Time series of the accuracy of the statistical and CNN SAR water masks for IWL1 and IWL2 are shown in Figures 3b, 3d, 3f and 3h. In general, Sentinel-1 VV results (0.9 probability threshold) are slightly more accurate than Sentinel-1 VH polarization results (0.7 probability threshold), which in turn are slightly more accurate than TerraSAR-X HH polarization results (0.9 probability threshold). Similarly to TSF1 and TSF2, there is a higher accuracy for all datasets during dry periods and lower accuracy when there is a significant amount of ponding and/or saturated material as identified by NDWI and MNDWI.

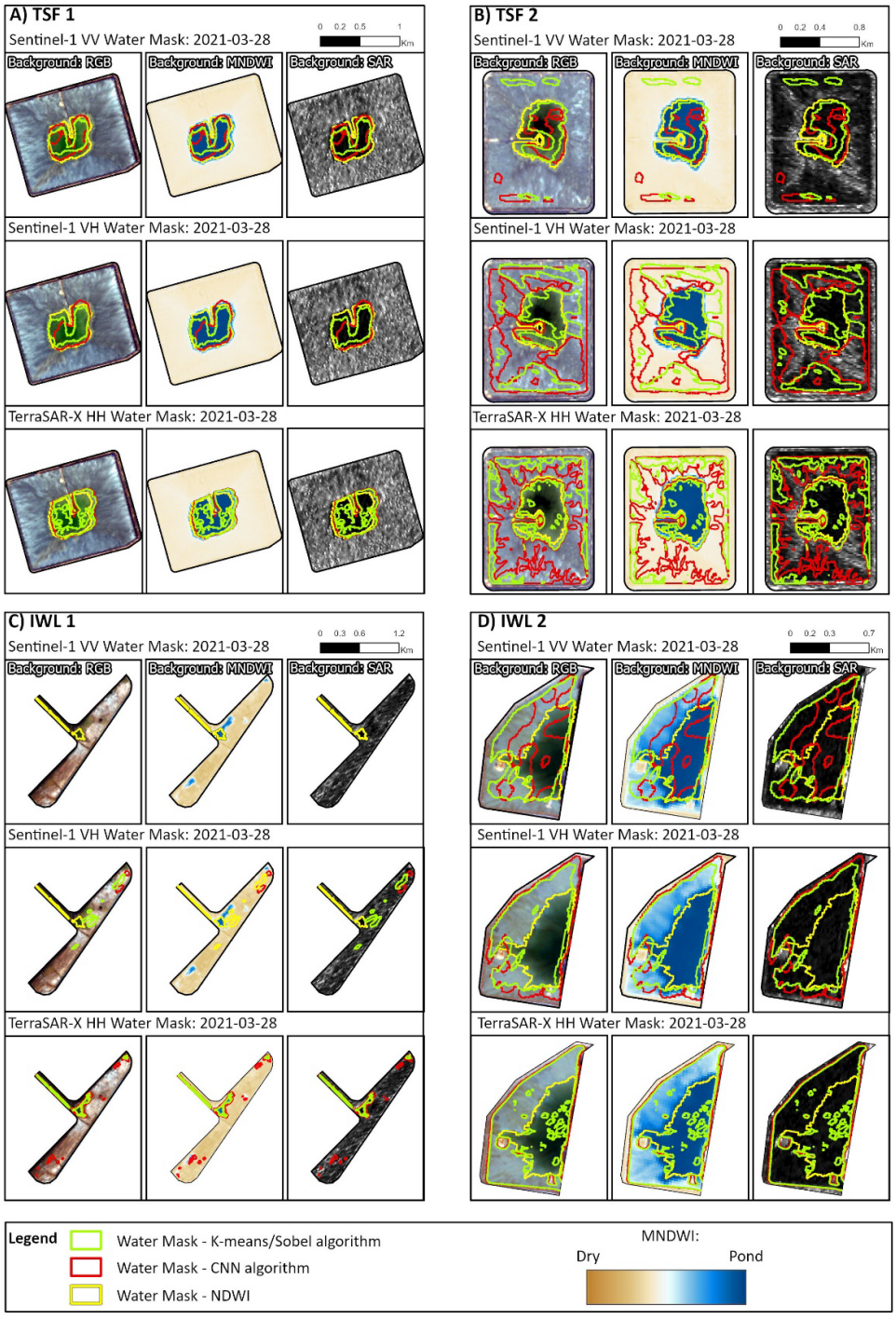

Figure 4: Water mask extent polygons produced using the k-means/Sobel and CNN algorithms (SAR data) and k-means/Sobel (NDWI) overlaid over true color (labelled RGB), MNDWI and SAR amplitude rasters for A) TSF1; B) TSF2; C) IWL1; D) IWL2

The low accuracy of the SAR water masks during periods of high-water content is explained by the algorithm often classifying wet beach areas as water, therefore there are many false positives since the reference water masks correspond only to supernatant ponds as classified by NDWI. This is likely due to the lack of contrast between wet material and pond areas in the SAR amplitude data for some acquisitions (e.g., SAR amplitude panel in Figure 4d). The notable discrepancies between the Sentinel-1 VH results and the other polarizations are limited to one of two TSF categories presented in this study (i.e., TSF1 and TSF2) and occur within a specific period (Figures 2a, 2c, 2e and 2g). This may suggest that specific types of material deposited within these TSFs may be indistinguishable from moisture in the VH polarization with the statistical and CNN algorithms used.

This preliminary CNN algorithm proved to be successful at detecting TSF moisture despite being trained on very different water bodies such as lakes and with data limited to Sentinel-1 in the VV polarization. Differences in the backscatter properties of SAR are expected to be significant between natural water bodies and tailings due to sediment content and water depth, as are differences in the spatial distribution and the saturation gradient around standing water. Based on the results of this analysis, a CNN trained on TSFs may be able to better discriminate between wet beach and supernatant ponds.

Integration of water mapping and InSAR monitoring results

In this section, InSAR is used in conjunction with supernatant pond and saturation mapping to demonstrate the relationship between TSF activity and embankment stability, with a focus on the integrated waste landforms. Embankment stability can be affected by variations in moisture content. Moisture from the material deposited in the TSFs can saturate the embankment, increasing pore pressure and therefore the stresses acting on the embankment. Increased moisture content also increases the weight of the tailings, which can negatively impact embankment stability, as well as settling of the material (Han et al., 2012; Dimitrova and Yanful, 2011). Finally, dry conditions leading to desiccation, cracking and erosion, can also undermine the stability of the embankment (e.g., Vardon, 2015).

The SqueeSAR algorithm provides measurements over areas where the natural radar targets on the ground surface have not changed significantly over time – areas with significant surface changes will contain gaps in data coverage. IWL1 was constructed during the first 6 months of the analysis period, therefore the SqueeSAR analysis resulted in displacement measurements only on the undisturbed portions of the embankments. IWL2 was constructed prior to the start of the SqueeSAR analysis. At IWL1, two areas of subsidence are identified (Figure 5a). The displacement history is similar for both, with three main phases of subsidence as follows: (A) slow average displacement velocity (-9 mm/yr) from approximately January 2021 to January 2022; (B) increased displacement velocity (-24 mm/yr) from approximately January 2022 to July 2023; (C) decreased displacement velocity (-12 mm/yr) from approximately July 2023

to the end of the analysis in February 2024 (Figure 5c). Fifty-three mm of cumulative subsidence are measured over the analysis period.

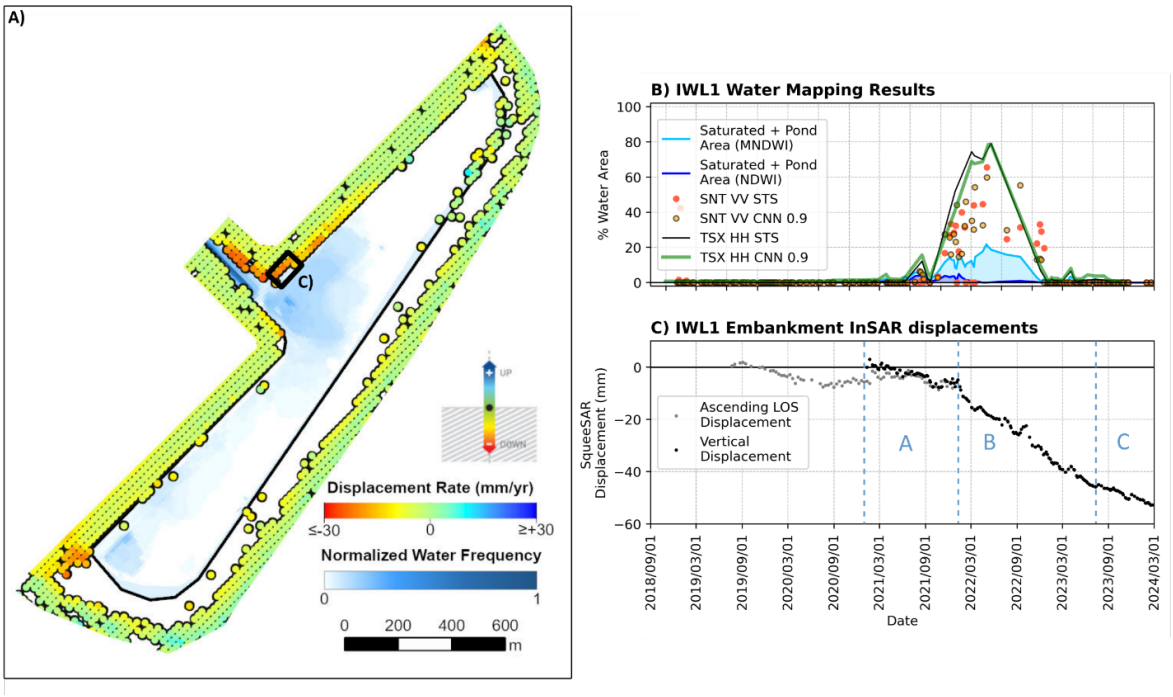

Figure 5: A) Points represent the average velocity of the multi-temporal InSAR analysis on the embankments of IWL1. Colors within the TSF represent the normalized frequency at which each pixel was classified as water during the analysis period using NDWI (1 being the most frequent). B) Percentage water area mapped within this TSF using MS and SAR data. C) Average time series of displacement at the location denoted by thick black polygon in A)

For IWL1, while the main ponding areas shown in Figure 5a correspond to the higher displacement areas, the relationship between the prolonged period of higher InSAR velocity (phase B) and the relatively short period of supernatant ponding is not straightforward. However, the period of increased % area of combined saturated and water pixels (based on MNDWI pixels > 0.1 and SAR-derived water classification) has a similar time scale (Figure 5b), only the phase B InSAR velocity increase is delayed by approximately 6 months. The supplementary monitoring of saturated material rather than ponding only may therefore provide valuable information on the interplay between TSF activity and embankment instability.

An area of subsidence was also identified at IWL2, as shown in Figure 6a. The main phases of displacement are as follows: (A) relatively low average velocity (-13 mm/yr) from the beginning of the analysis (January 2021) to approximately August 2021; (B) higher average velocity (-40 mm/yr) from approximately August 2021 to March 2022; (C) lower velocity (-18 mm/yr) from approximately March 2022 to August 2022; (D) higher velocity (-51 mm/yr) from approximately August 2022 to January 2023;

and (E) lower average velocity (-17 mm/yr) and gradual deceleration from approximately January 2023 to the end of the analysis period (Figure 6c). Eighty mm of subsidence occurred throughout the analysis period.

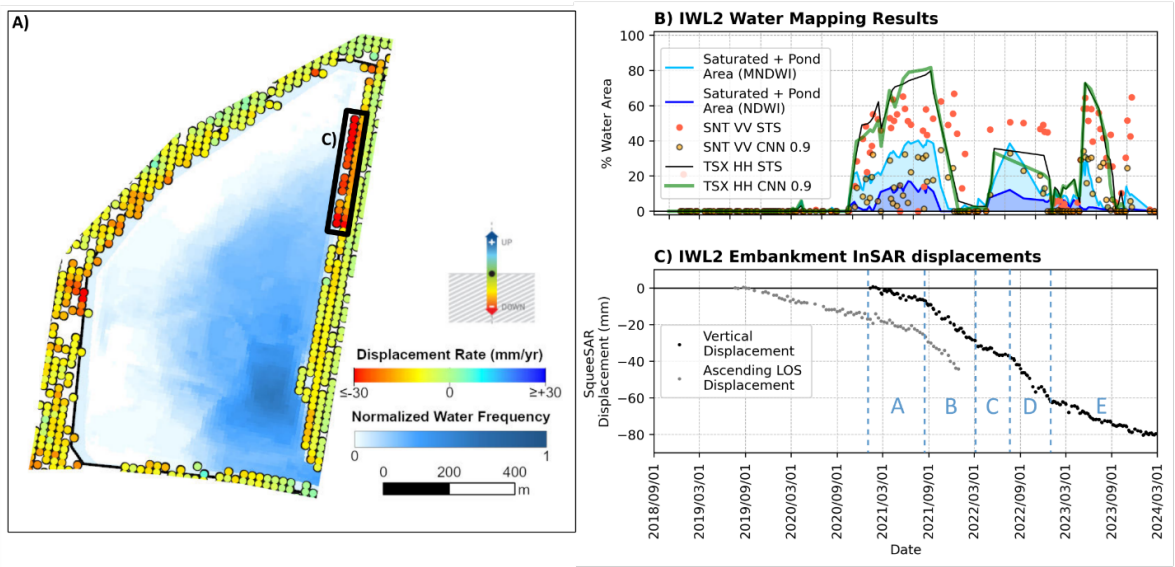

Figure 6: A) Points represent the average velocity of the multi-temporal InSAR analysis on the embankments of IWL2. Shades of blue within the TSF represent the normalized frequency at which each pixel was classified as water during the analysis period using NDWI (1 being the most frequent). B) Percentage water area mapped within this TSF using MS and SAR data. C) Average time series of displacement at the location denoted by thick black polygon in A)

Similarly to IWL1, the less stable portion of the IWL2 embankment is in proximity of an area frequently classified as water (Figure 6a). Furthermore, there are higher InSAR velocity periods starting a few months after periods with large areas covered by ponds and saturated material (Figure 6b). The delay may be related to the gradual change in the stress field due to the saturation and increase of pore pressure of the embankment reducing its shear strength, and other factors such as the weight of the settled tailings, seepage leading to embankment erosion, or the draining of water away from the IWL (Clarkson and Williams, 2021; Saad and Mitri, 2011).

These results illustrate the complementarity of surface water indices, SAR amplitude data and multi-temporal InSAR in monitoring and assessing the impact of the TSF operations on embankment instability. While remote sensing methods can provide long-term history of data over large areas, determining the exact deformation mechanisms in play in the locations identified by InSAR and their causes will require input from the mine operator on their operational schedules and in-situ measurements such as pore pressure, tilting and settlement data, and signs of cracking and tension.

Conclusion

This study demonstrates the ability of two ML algorithms (i.e., a k-means/Sobel operator approach and a preliminary CNN trained on lakes and rivers with VV-polarized SAR data) to identify saturated material within TSFs using SAR amplitude imagery alone. The outcomes are impactful, as well-established methods of detecting TSF moisture and ponding rely on MS imagery that can be heavily impacted by cloud cover.

The results outline specific recommendations for the use of these algorithms in monitoring TSF moisture. Firstly, although further refinement is required to accurately discriminate between fully saturated tailings and standing water, the ML algorithms using SAR data were able to detect large areas corresponding to the combined saturated and pond areas detected by MNDWI. Secondly, the choice of SAR data polarization, and potentially the wavelength (and therefore spatial resolution), significantly affect the results. Of the datasets used in this analysis, Sentinel-1 VV and TerraSAR-X HH-polarized data were generally more successful at mapping TSF moisture than Sentinel-1 VH polarized data. The spatial and temporal trends of saturated material detected using Sentinel-1 VV and TerraSAR-X HH data are also shown to be useful in interpreting TSF embankment displacements measured by InSAR, with periods of extensive saturated material followed by periods of faster embankment subsidence.

The accuracy of the CNN in mapping supernatant ponds is expected to improve with a network trained on TSFs and a variety of SAR polarizations and resolutions. Additionally, information on the operational schedules and specific tailings material deposited is required to fully characterize the polarimetric properties of the TSFs.

References

Acharya, T.D., Subedi, A. and Lee, D.H. 2018. Evaluation of Water Indices for Surface Water Extraction in a Landsat 8 Scene of Nepal. *Sensors* 18: 2580.

Brisco, B., Kapfer, M., Hirose, T., Tedford, B. and J. Liu. 2011. Evaluation of C-band polarization diversity and polarimetry for wetland mapping. *Canadian Journal of Remote Sensing* 37: 82–92.

Cacciuttolo, C. and Cano, D. 2023. Spatial and temporal study of supernatant process water pond in tailings storage facilities: Use of remote sensing techniques for preventing mine tailings dam failures. *Sustainability* 15(6): 4984.

Clarkson, L. and Williams, D. 2021. An overview of conventional tailings dam geotechnical failure mechanisms. *Mining, Metallurgy and Exploration* 38(3): 1305–1328.

Dimitrova, R.S. and Yanful, E.K. 2011. Undrained strength of deposited mine tailings beds: Effect of water content, effective stress and time of consolidation. *Geotechnical and Geological Engineering* 29: 935–951.

Ferretti, A. 2014. *Satellite InSAR Data: Reservoir Monitoring from Space*. EAGE.

Ferretti, A., Fumagalli, A., Novali, F., Prati, C., Rocca, F. and Rucci, A. 2011. A new algorithm for processing interferometric data-stacks: SqueeSAR. *IEEE Transactions on Geoscience and Remote Sensing* 49(9): 3460–3470.

Gao, B.C., 1996. NDWI—A normalized difference water index for remote sensing of vegetation liquid water from space. *Remote Sensing of Environment* 58(3): 257–266.

Han, J., Bhandari, A. and Wang, F. 2012. DEM analysis of stresses and deformations of geogrid-reinforced embankments over piles. *International Journal of geomechanics* 12(4): 340–350.

Jiang, J., Sun, H., Wang, Y., Cacciuttolo, C. and Cano, D. 2023. Spatial and temporal study of supernatant process water pond in tailings storage facilities: use of remote sensing techniques for preventing mine tailings dam failures. *Sustainability* 15(6): 4984.

Kanopoulos, N., Vasanthavada, N. and Baker, R. L. 1988. Design of an image edge detection filter using the Sobel operator. *IEEE Journal of Solid-State Circuits* 23(2):358–367.

Koleshwar, A., Tortini, R. and Falorni, G. 2023. Assessing tailings consolidation and changes in supernatant pond area using InSAR and the normalised difference moisture index. In G.W. Wilson, N.A. Beier, D.C. Sego, A.B. Fourie and D. Reid (editors), *Paste 2023. Proceedings of the 25th International Conference on Paste, Thickened and Filtered Tailings.* University of Alberta, Edmonton, and Australian Centre for Geomechanics, Perth: 765–775.

Lattari, F., Gonzalez Leon, B., Asaro, F., Rucci, A., Prati, C. and Matteucci, M. 2019. Deep learning for SAR image despeckling. *Remote Sensing* 11(13): 1532.

Piciullo, L., Storrøsten, E.B., Liu, Z., Nadim, F. and Lacasse, S. 2022. A new look at the statistics of tailings dam failures. *Engineering Geology* 303: 106657.

Robinove, C.J. 1981. The logic of multispectral classification and mapping of land. *Remote Sensing of Environment* 11(C): 231–244.

Saad, B. and Mitri, H. 2011. Hydromechanical analysis of upstream tailings disposal facilities. *Journal of Geotechnical and Geoenvironmental Engineering* 137(1) :27–42.

Townshend, J., Justice, C., Li, W., Gurney, C. and McManus, J. 1991. Global land cover classification by remote sensing: present capabilities and future possibilities. *Remote Sensing of Environment* 35(2–3): 243–255.

Vardon, P.J., 2015. Climatic influence on geotechnical infrastructure: A review. *Environmental Geotechnics* 2(3): 166–174.

Xu, H. 2006. Modification of normalised difference water index (NDWI) to enhance open water features in remotely sensed imagery. *Int. J. Remote Sens*. 27: 3025–3033.